Joule

CellPress

Article

# A high-voltage and stable zinc-air battery enabled by dual-hydrophobic-induced proton shuttle shielding

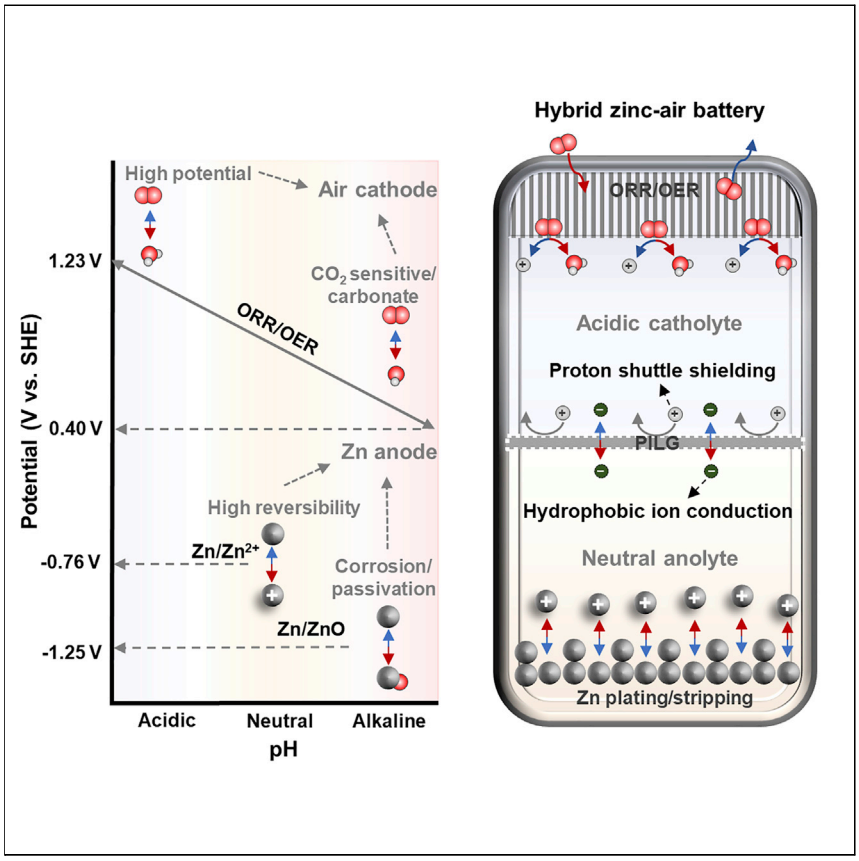


The long-standing challenges to the practical implementation of rechargeable zinc-air batteries (ZABs) are the electrochemical irreversibility of zinc (Zn) anode (passivation/corrosion) and degradation of the air cathodes (clogged carbonation) in alkaline electrolyte, which eventually results in poor cycle life and low cell voltage. To overcome these open problems, a hybrid ZAB has been achieved by decoupling the highly reversible neutral Zn anode and high-voltage/carbonate-free acidic air cathode via a dual-hydrophobic-induced proton-shuttle-shielding and hydrophobic $TFSI^-$-conducting membrane.

Yang-feng Cui, Yun-hai Zhu, Jia-yi Du, ..., Wan-qiang Liu, Gang Huang, Xin-bo Zhang

xbzhang@ciac.ac.cn

## Highlights

This work reports a hybrid neutral-acidic ZAB

This work proposes a proton-shuttle-shielding and hydrophobic-ion-conducting mechanism

The hybrid ZAB shows a high working voltage and stable operation

Cui et al., Joule 6, 1–15
July 20, 2022 
https://doi.org/10.1016/j.joule.2022.05.019

Please cite this article in press as: Cui et al., A high-voltage and stable zinc-air battery enabled by dual-hydrophobic-induced proton shuttle shielding, Joule (2022), https://doi.org/10.1016/j.joule.2022.05.019

Joule

CellPress

Article

# A high-voltage and stable zinc-air battery enabled by dual-hydrophobic-induced proton shuttle shielding

Yang-feng Cui,[1,2,5] Yun-hai Zhu,[1,3,5] Jia-yi Du,[1,4,5] Yong-lai Zhang,[1] Kai Li,[1] Wan-qiang Liu,[2] Gang Huang,[1] and Xin-bo Zhang[1,4,6,*]

## SUMMARY

**Rechargeable zinc-air batteries (ZABs) stand out among next-generation battery technologies due to their high energy density and high safety but suffer from electrochemical irreversibility. Herein, we report a hybrid ZAB with a long lifespan and high working voltage; it uses a neutral anolyte, an acidic catholyte, and a proton-shuttle-shielding dual-hydrophobic membrane to isolate the two electrolytes. The hybrid ZAB operates through the stable electrochemical plating and stripping of zinc (Zn) in a neutral anolyte and a high-voltage $O_2$ redox reaction in acidic catholyte. The designed proton-shuttle-shielding dual-hydrophobic membrane selectively transports hydrophobic bis(trifluoromethylsulfonyl) imide anions ($TFSI^-$) and effectively avoids the crossover of protons. As a result, the hybrid ZAB exhibits a high working voltage (1.50 V) and stable operation (up to 2,000.0 h) in ambient air. This strategy not only overcomes the severe irreversibility of conventional ZABs but also promotes development of electrolyte-decoupled systems.**

## INTRODUCTION

Rechargeable zinc-air batteries (ZABs) stand out among next-generation battery technologies for their potentially low cost, high safety, environmental friendliness, and high energy density.[1–5] The long-standing challenges to the practical implementation of rechargeable ZABs are the electrochemical irreversibility of the zinc (Zn) anode and the degradation of the air cathodes in the alkaline electrolyte, which eventually results in poor cycle life and low cell voltage.[6–10] To improve the reversibility of ZABs, exhaustive efforts have been made to exploit highly survivable catalysts for use in air cathodes and minimize the corrosion of Zn anodes through electrode architecture design or electrolyte additives.[11–16] Although significant improvements have been achieved, the fundamental core challenges that come from the alkaline electrolyte must still be overcome.

Recent efforts have demonstrated that the near neutral aqueous electrolytes could maintain highly reversible Zn stripping/plating behavior, which enables the Zn anode with long life span.[17–21] However, owing to the low standard potential of Zn anode (−0.76 V versus SHE, standard hydrogen electrode) and the sluggish kinetics of oxygen reduction reaction/oxygen evolution reaction (ORR/OER) in neutral electrolytes, the neutral ZAB exhibits unsatisfied performance, especially the low cell voltage of ~1.00 V.[22] Theoretically, the strongly acidic electrolytes enable the air cathode with a more positive potential of nearly 1.23 V versus SHE and

## Context & scale

As a century-old technology, the zinc-air battery shows the potential advantages of low cost, high safety, environmental friendliness, and high energy density. In addition, the primary zinc-air battery has been introduced to the commercial market since 1932. However, its rechargeability is still limited by severe side reactions, which eventually results in the poor cycle life. To realize the high rechargeability of zinc-air battery, this work reports a hybrid zinc-air battery by decoupling the neutral zinc anode and acidic air cathode via the proposed proton-shielding and hydrophobic-ion-conducting membrane, which realizes a stable battery cycling of 2,000 h far beyond the traditional zinc-air batteries. In addition, the proposed hybrid system could create a development direction of high-performance energy storage systems.

Please cite this article in press as: Cui et al., A high-voltage and stable zinc-air battery enabled by dual-hydrophobic-induced proton shuttle shielding, Joule (2022), https://doi.org/10.1016/j.joule.2022.05.019



simultaneously immune to $CO_2$ poisoning issues[23,24]; although it inevitably accelerates the corrosion of Zn anode. Herein, we propose a hybrid ZAB by decoupling the working conditions of the air cathode and Zn anode so as to make both acidic ORR/OER and neutral Zn redox reactions in a single cell, which could theoretically endow ZABs with long cycle life and a high working voltage of 1.99 V.

Unfortunately, like most decoupling electrolyte systems, this hybrid cell faces the complicated challenges in preventing chemical crossover between the two different electrolytes. Once the protons in the catholyte spread to the neutral anolyte, the Zn anode will be consumed irreversibly. Conventional ion exchange membranes (IEMs) strategies could alleviate but do not fundamentally solve the cross-contamination of decoupling electrolytes,[25–27] since the water-permeable membranes were easily permeated by hydrophilic ions, like protons.[28–30] Herein, we proposed and designed a dual-hydrophobic-induced proton-shuttle-shielding and hydrophobic-ion-conducting membrane for this hybrid ZAB by incorporating the hydrophobic ionic liquid (IL) and graphene into the hydrophobic polymer matrix (polymer/IL/graphene [PILG]). Such a PILG membrane selectively transports hydrophobic bis(trifluoromethylsulfonyl)imide anions ($TFSI^-$) and effectively and long lastingly avoids the crossover of protons. As a result, the designed dual-hydrophobic PILG enables the hybrid ZAB to achieve unprecedented performance breakthroughs in rechargeable ZABs, including a high open-circuit voltage (OCV) of 1.78 V (higher than the theoretical potential of conventional alkaline ZABs: 1.66 V), high working voltage (1.50 V), stable operations (up to 2,000.0 h with slight pH fluctuation of anolyte from 5.41 to 4.52), and high Zn utilization (>97.0%) in ambient air than its alkaline counterparts, originating from highly electrochemical reversibility of both Zn anode and air cathode.

## RESULTS

### Cell design

The proposed hybrid ZAB is made up of two reaction chambers isolated by a proton-shuttle-shielding dual-hydrophobic membrane composed of an IL and graphene in poly(vinylidene fluoride-co-hexafluoropropylene) (PVDF-HFP), as illustrated in Figure 1. The neutral reaction chamber contains an anolyte ($ZnSO_4$ (zinc sulfate) + LiTFSI [bis(trifluoromethane)sulfonimide lithium salt]) and a metallic Zn anode, and the acidic reaction chamber consists of a catholyte ($H_2SO_4$ (sulfuric acid) + LiTFSI) and an air cathode loaded with commercial Pt/C + $IrO_2$ catalysts (Figure S1). The PILG membrane allows conduction of the $TFSI^-$ ions to balance the charges and prevents proton crossover from the catholyte to the anolyte during battery operation. Upon discharge, the ORR occurs at the air cathode and forms water molecules in the acidic catholyte, and $Zn^{2+}$ ions are stripped from the Zn anode and dissolved in the neutral anolyte. Meanwhile, the $TFSI^-$ ions pass through the PILG from the catholyte to the anolyte. The water molecules are oxidized to $H^+$ ions and $O_2$ molecules, whereas the dissolved $Zn^{2+}$ ions are deposited on the anode surface during charging. The transferred $TFSI^-$ ions simultaneously return to the catholyte from the anolyte. This hybrid system not only uses a superior neutral electrolyte for stable Zn plating/stripping but also enables a carbonate-free air cathode with a high working voltage due to the acidic environment. The two isolated reactions of neutral Zn dissolution/deposition and the acidic ORR/OER are implemented in such a hybrid system, and the respective and total reactions are as follows.

$$\text{Neutral anolyte: } Zn \leftrightarrow Zn^{2+} + 2e^- \ (E_o = -0.76 \text{ V versus SHE})$$

$$\text{Acidic catholyte: } O_2 + 4H^+ + 4e^- \leftrightarrow 2H_2O \ (E_o = 1.23 \text{ V versus SHE})$$

[1]State Key Laboratory of Rare Earth Resource Utilization, Changchun Institute of Applied Chemistry, Chinese Academy of Sciences, Changchun 130022, China

[2]School of Materials Science and Engineering, Changchun University of Science and Technology, Changchun 130022, China

[3]Key Laboratory of Automobile Materials (Jilin University), Ministry of Education, Department of Materials Science and Engineering, Jilin University, Changchun 130022, China

[4]School of Applied Chemistry and Engineering, University of Science and Technology of China, Hefei 230026, China

[5]These authors contributed equally

[6]Lead contact

*Correspondence: xbzhang@ciac.ac.cn

https://doi.org/10.1016/j.joule.2022.05.019

Please cite this article in press as: Cui et al., A high-voltage and stable zinc-air battery enabled by dual-hydrophobic-induced proton shuttle shielding, Joule (2022), https://doi.org/10.1016/j.joule.2022.05.019





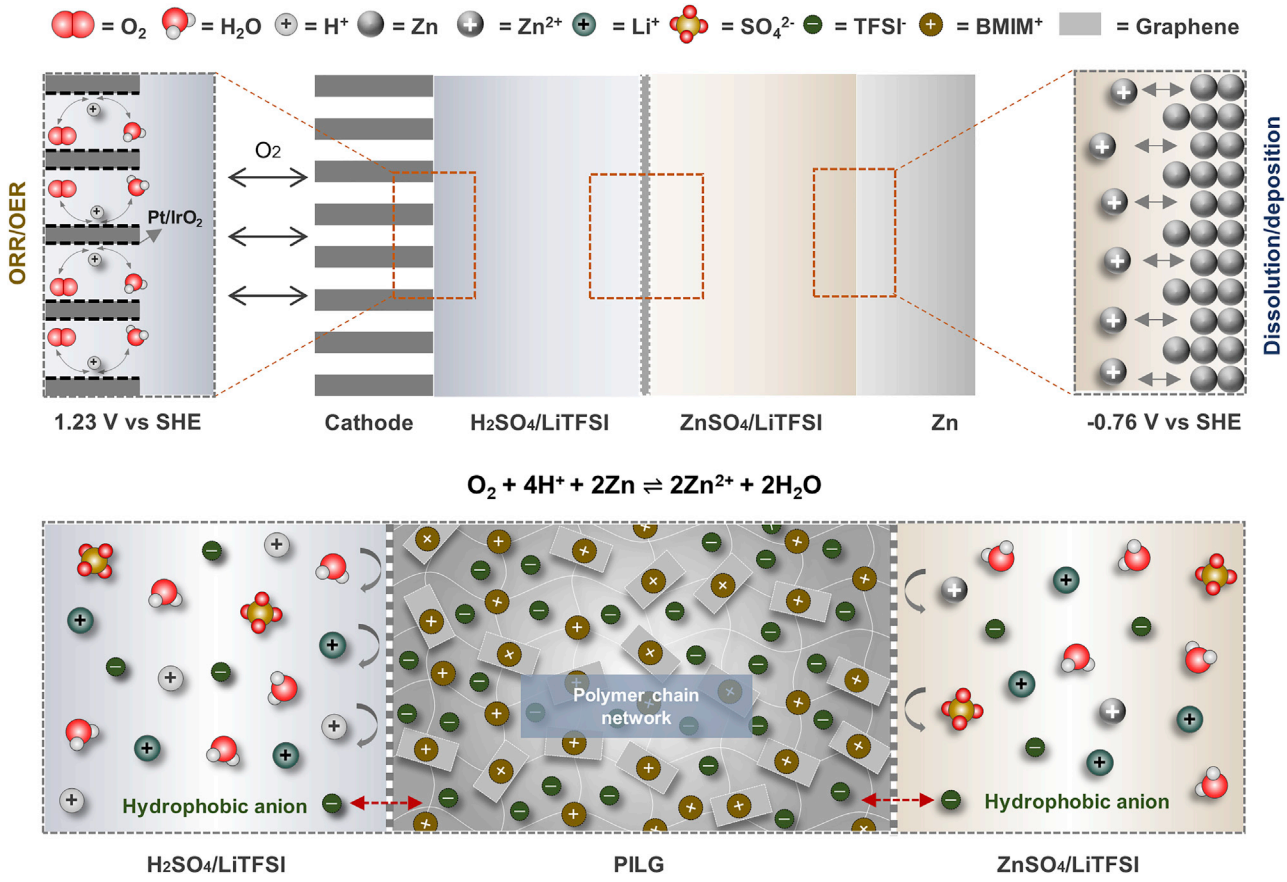


**Figure 1. Proposed hybrid ZAB**

Schematic diagram of the cell structure with proton-shuttle-shielding and $TFSI^-$-conducting membrane and the corresponding chemical reactions.

Total reaction: $O_2 + 4H^+ + 2Zn \leftrightarrow 2H_2O + 2Zn^{2+}$ ($E_{total}$ = 1.99 V)

Although the standard potential provided by the Zn anode in the neutral electrolyte (−0.76 V versus SHE) is lower than that of the alkaline electrolyte (−1.25 V versus SHE) due to the different electrochemical reactions, the standard potential of the ORR/OER in the acid catholyte is sufficient to compensate for the voltage loss of the anode, thus making the overall theoretical voltage of the hybrid ZAB (1.99 V) higher than that of the conventional alkaline ZAB (1.65 V; Figure S2).

## Crossover of protons in hybrid ZABs

To create this new hybrid system, we assembled hybrid ZABs with commercial anion exchange membrane (AEM, Fumasep FAB-PK-130) and cation exchange membrane (CEM, Nafion N117) (Figure S3). The AEM-based hybrid ZAB consisted of a $H_2SO_4$ catholyte and $ZnSO_4$ anolyte, wherein the AEM allowed penetration of $SO_4^{2-}$ ions to balance the charge of the catholyte and anolyte.[31] Unlike the AEM-based hybrid ZAB, the CEM-based hybrid ZAB consisted of a $H_2SO_4$ + $Li_2SO_4$ catholyte and a $ZnSO_4$ + $Li_2SO_4$ anolyte, wherein the CEM allowed penetration of $Li^+$ ions to balance the charge.[32] Using a homemade *in situ* pH-monitoring cell (Figure S4A), we then tested the battery performance and tracked the pH of the anolyte upon battery operation. Benefiting from the high voltage of the $O_2$ redox reaction in acidic

Please cite this article in press as: Cui et al., A high-voltage and stable zinc-air battery enabled by dual-hydrophobic-induced proton shuttle shielding, Joule (2022), https://doi.org/10.1016/j.joule.2022.05.019



catholytes, both hybrid ZABs displayed high OCVs above 1.60 V (Figure S5) and discharge voltage of nearly 1.50 V in the initial several cycles (Figures S4B and S4C). However, the pH of the two anolytes sharply decreased during the first 3.0 h and then remained at nearly 1.50. As a result, chemical corrosion of the Zn anode ($Zn + 2H^+ \rightarrow Zn^{2+} + H_2$) occurred in the anolyte chambers. In the end, the batteries suffered premature death with a very limited cycle life of approximately 70.0 h because the Zn anode was exhausted (Figures S4D and S4E). There was no obvious change to the air cathodes after cycling (Figure S6), since the acidic catholyte did not form carbonate. The hybrid ZABs have absolute advantages over alkaline ZABs, including a high working voltage and carbonate-free air cathode. Nevertheless, the anticipated long-term cycling of the hybrid ZAB has not been achieved due to the insufficient proton-shuttle-shielding ability of IEMs (see Tables S1–S3).

### The proton-shielding and $TFSI^-$-conducting membrane as a separator

The essential prerequisite for the long-term operation of the hybrid ZAB is that the two reaction chambers work independently in their respective environments, thus requiring complete and long-lasting prevention of the crossover of protons. This cannot be achieved by conventional IEMs due to their water-immersible property since protons exist in aqueous solution as hydrated ions.[33,34] Theoretically, the hydrophobic membrane could completely shield the proton shuttle; however, it also prevents the shuttling of other hydrophilic ions. Unlike the hydrophilic ions solvated by water molecules, hydrophobic ions are barely bound by water molecules, which may freely pass through the hydrophobic membrane in such an aqueous hybrid system. To this end, we decided to construct a dual-hydrophobic membrane using hydrophobic PVDF-HFP as the polymer framework and hydrophobic $TFSI^-$ ions from the IL (1-butyl-3-methylimidazolium bis(trifluoromethylsulfonyl)imide, denoted as [BMIM][TFSI]) as conducting ions. This polymer/IL (PIL) membrane was constructed through a sol-gel method (left Figure 2A). Theoretically, the IL could have the characteristics of both high hydrophobicity and ionic conductivity (Figure S7),[35,36] which could be beneficial for such a hybrid battery to build a proton-shuttle-shielding system. To determine whether it is possible, we first optimized the ratio between the IL and PVDF-HFP, and a series of PILs with different IL contents (from 30 wt% to 60 wt%) were synthesized. Among them, the prepared $PIL_{50}$ (the content of IL reaches 50 wt %) showed the densest and smoothest surface (Figures 2C and S8) and exhibited a high ion conductivity of up to 0.76 mS $cm^{-1}$ (Figure S9). Therefore, a hybrid ZAB based on $PIL_{50}$ with an anolyte containing 0.5 M $ZnSO_4$ + 1.0 M LiTFSI and catholyte containing 0.5 M $H_2SO_4$ + 1.0 M LiTFSI was fabricated to test the battery performance and proton-shuttle-shielding effect (Figure S12A). The 0.5 M $ZnSO_4$ + 1.0 M LiTFSI electrolyte was the best neutral electrolyte among the electrolyte salts tested at different concentrations, which afforded a cycle life of 1,000.0 h; the battery did not short circuit, and the Zn stripping/plating behavior was stable, with an average Coulombic efficiency (CE) of 99.53% (Figures S10 and S11). Compared with the CEM (cycling 72.5 h; Figure S4B) and AEM (cycling 70.5 h; Figure S4C), the $PIL_{50}$ enabled a longer cycle life of 365.5 h for a hybrid ZAB (Figure S12B), indicating improved proton-shuttle-shielding capability. However, the pH of the anolyte also slowly decreased to approximately 2 as the battery operated for the first 70 h (Figure S12B), indicating that some protons still passed through the PIL from the catholyte into the anolyte. This result was further confirmed by the exhaustion of the Zn anode in the failed battery (see inset of Figure S12B).

To explore the reasons for the failure of the $PIL_{50}$, we then measured the mass variation of the $PIL_{50}$ after it was soaked in catholyte and anolyte. Surprisingly, the mass loss of $PIL_{50}$ was more than 10.0 wt% after merely soaking for 48.0 h and increased to

Please cite this article in press as: Cui et al., A high-voltage and stable zinc-air battery enabled by dual-hydrophobic-induced proton shuttle shielding, Joule (2022), https://doi.org/10.1016/j.joule.2022.05.019





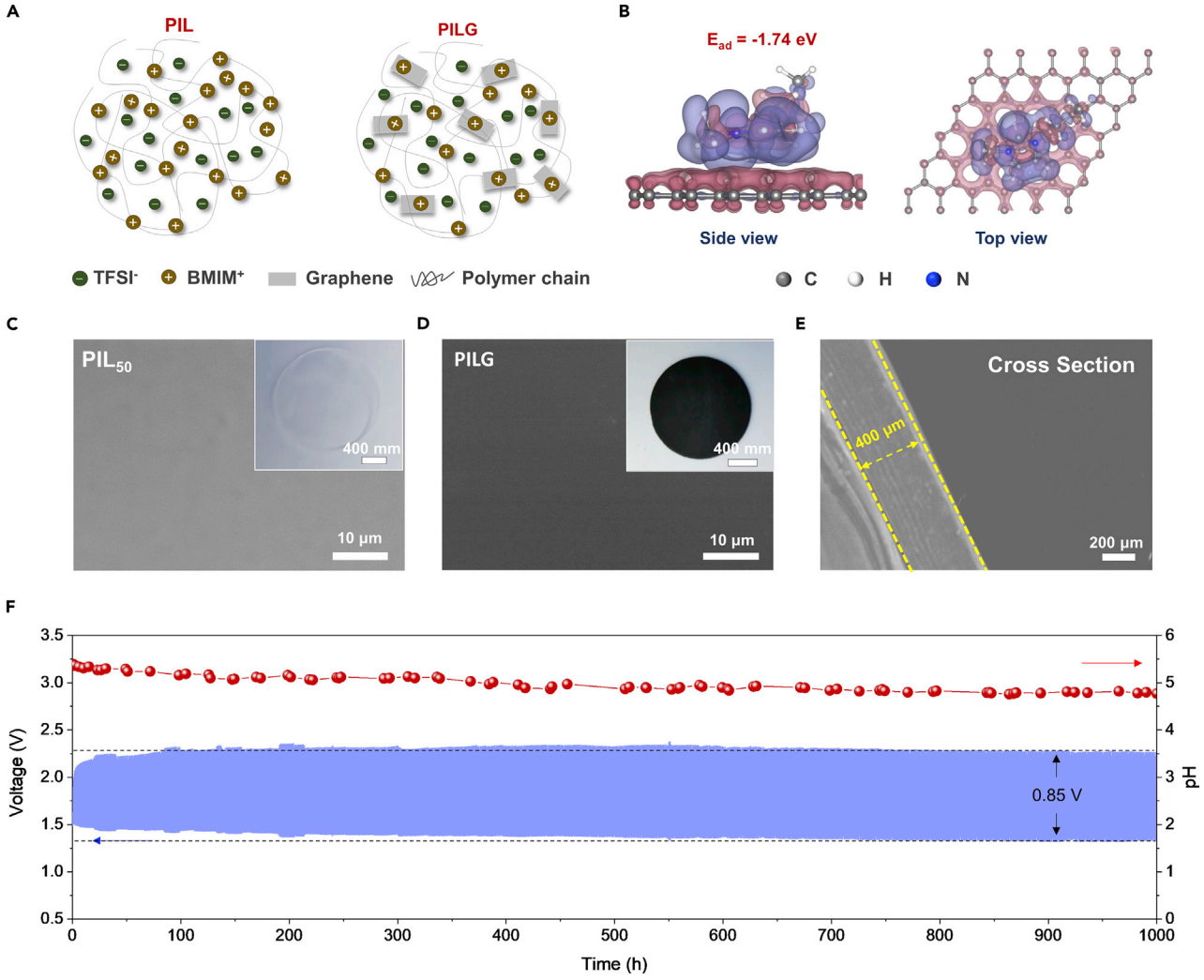


**Figure 2. Preparation and characterization of the PILG membrane**

(A) Schematic of the PIL and PILG structures.

(B) Charge density difference of one $BMIM^+$ ion adsorbed on graphene.

(C) SEM image of the top view of the $PIL_{50}$ (scale bar, 10 μm), inset showing the optical picture (scale bar, 400 mm).

(D) SEM image of the top view of the PILG (scale bar, 10 μm), inset showing the optical picture (scale bar, 400 mm).

(E) SEM image of the side view of the PILG (scale bar, 200 μm).

(F) Cycling performance and pH variation of the hybrid ZAB with the PILG at 0.5 mA $cm^{-2}$ and 1 h for per cycle.

23.5 wt% as the soaking time was prolonged to 14 days (Figure S13A), meaning that the IL leaked from the $PIL_{50}$ into the catholyte. The same phenomenon also occurred when the $PIL_{50}$ was soaked in the anolyte (Figure S13A). The soaking experiment revealed that the leakage of IL was responsible for the failure of the hybrid ZAB, since the discontinuous hydrophobic phase (IL) in the PIL caused the acidic catholyte to penetrate the anolyte and then corrode the Zn anode (Figure S13B). Notably, the adsorption energy ($E_{ad}$) between the 1-butyl-3-methylimidazolium cation ($BMIM^+$) and the PVDF-HFP matrix is extremely low (maximum value: −0.24 eV; Figure S13C) according to density functional theory (DFT) calculations, which may be the underlying reason for IL leakage from the PIL.

Due to the potentially strong physical absorption through π-π interactions between $BMIM^+$ of IL and $C_6$ surface of graphene,[37,38] we decided to introduce graphene into

Please cite this article in press as: Cui et al., A high-voltage and stable zinc-air battery enabled by dual-hydrophobic-induced proton shuttle shielding, Joule (2022), https://doi.org/10.1016/j.joule.2022.05.019



the PIL (PILG; right Figure 2A) to eliminate the issue of IL leakage. A gel was formed by homogeneously mixing graphene and the IL, and the structure of this gel was stable as the graphene content reached 1.50 wt% (Figure S14). This result indicates that only 1 mg of graphene was needed to enfold approximately $3 \times 10^{19}$ molecules of [BMIM][TFSI] to generate a stable gel. DFT calculations further revealed the high $E_{ad}$ between the $BMIM^+$ ion and graphene (up to −1.74 eV) as the electrons accumulated in the intermediate region between the $BMIM^+$ and graphene (Figure 2B), so that the incorporation of graphene could theoretically enhance the stability of the PIL.

According to the above analysis, PILG was prepared using the optimized ratio (1 g of PVDF-HFP, 1 g of [BMIM][TFSI] and 15 mg of graphene). Scanning electron microscopy (SEM) images show a smooth and nonporous PILG surface (Figure 2D; Figures S15A and S15B) with a thickness of nearly 400 μm (Figure 2E). Fourier transform infrared spectroscopy (FTIR) and Raman spectroscopy revealed the successful incorporation of the IL and graphene into the PVDF-HFP matrix (Figures S15C and S15D). Compared with the PIL, the PILG exhibited enhanced hydrophobic characteristics (Figures S16A–S16C) and an ion conductivity of 1.70 mS $cm^{-1}$ (Figure S16D; Table S4). In addition, the PILG showed the robust mechanical property with a fracture stress of 9.9 MPa and an elongation of 870% (Figures S17 and S18A) and the high thermal stability with a melting point of 101.2°C (Figure S18B) and a decomposition temperature of 424.5°C (Figures S18C and S18D). To further confirm the stability of the PILG, we then measured the mass variation of the PILG after soaking it in the catholyte and anolyte. The weight losses of the PILG were only 6.54 wt% and 4.90 wt% after soaking in the catholyte and anolyte for up to 30 days, respectively; these losses were much less than those of the $PIL_{50}$ (Figure S13A) in the same electrolytes (Figure S19A). Furthermore, strong absorption peaks belonging to [BMIM][TFSI] were detected in the FTIR spectra of soaked PILG (Figure S19B). This result indicates that the incorporation of graphene has significantly improved the stability of the PILG. Notably, the mass loss of the PILG was due to the slight dissolution of the IL from the PILG to the electrolyte. This dissolution phenomenon is completely suppressed by the IL-saturated electrolyte, since the mass loss of the PILG was nearly 0.00 wt% even after soaking in IL-saturated electrolyte for 30 days (Figure S19A). Additionally, to confirm the proton-shuttle-shielding effect of the PILG, we monitored the pH of the anolyte in the hybrid ZAB with the PILG as the separator (Figure 2F). As expected, the anolyte had a stable pH from 5.38 for the pristine material to 4.77 even after cycling for 1,000.0 h, and the hybrid ZAB exhibited stable charge/discharge behavior with a smaller polarization voltage of 0.85 V. This result indicated that our proton-shuttle-shielding PILG could fundamentally meet the essential challenge of IEMs for the proposed hybrid ZABs.

### The hydrophobic $TFSI^-$-conducting process

It should be noted that in the real environment of the designed hybrid ZAB, $Zn^{2+}$, $Li^+$, $SO_4^{2-}$, and $TFSI^-$ ions coexist in the anolyte, and $H^+$, $Li^+$, $SO_4^{2-}$, and $TFSI^-$ ions coexist in the catholyte. Since hydrophobic PILG merely allows dehydrated ions to pass, to reveal the conduction mechanism of PILG in the hybrid ZABs, we performed DFT calculations to determine the desolvation energy (DSE) of $M(H_2O)_n$ ($M = H^+$, $Li^+$, $Zn^{2+}$, $SO_4^{2-}$ and $TFSI^-$; Figure S20). Compared with the $H^+$, $Li^+$, $Zn^{2+}$, and $SO_4^{2-}$ ions, the $TFSI^-$ ion possessed an almost negligible DSE value of 0.05 eV (Figure 3A) due to the hydrophobicity of $TFSI^-$ (Figure S21). Thus, the "free" $TFSI^-$ ion is the most favorable charge carrier to balance the charge of the catholyte and anolyte because the large DSE values of other ions make the desolvation process extremely difficult.

Please cite this article in press as: Cui et al., A high-voltage and stable zinc-air battery enabled by dual-hydrophobic-induced proton shuttle shielding, Joule (2022), https://doi.org/10.1016/j.joule.2022.05.019





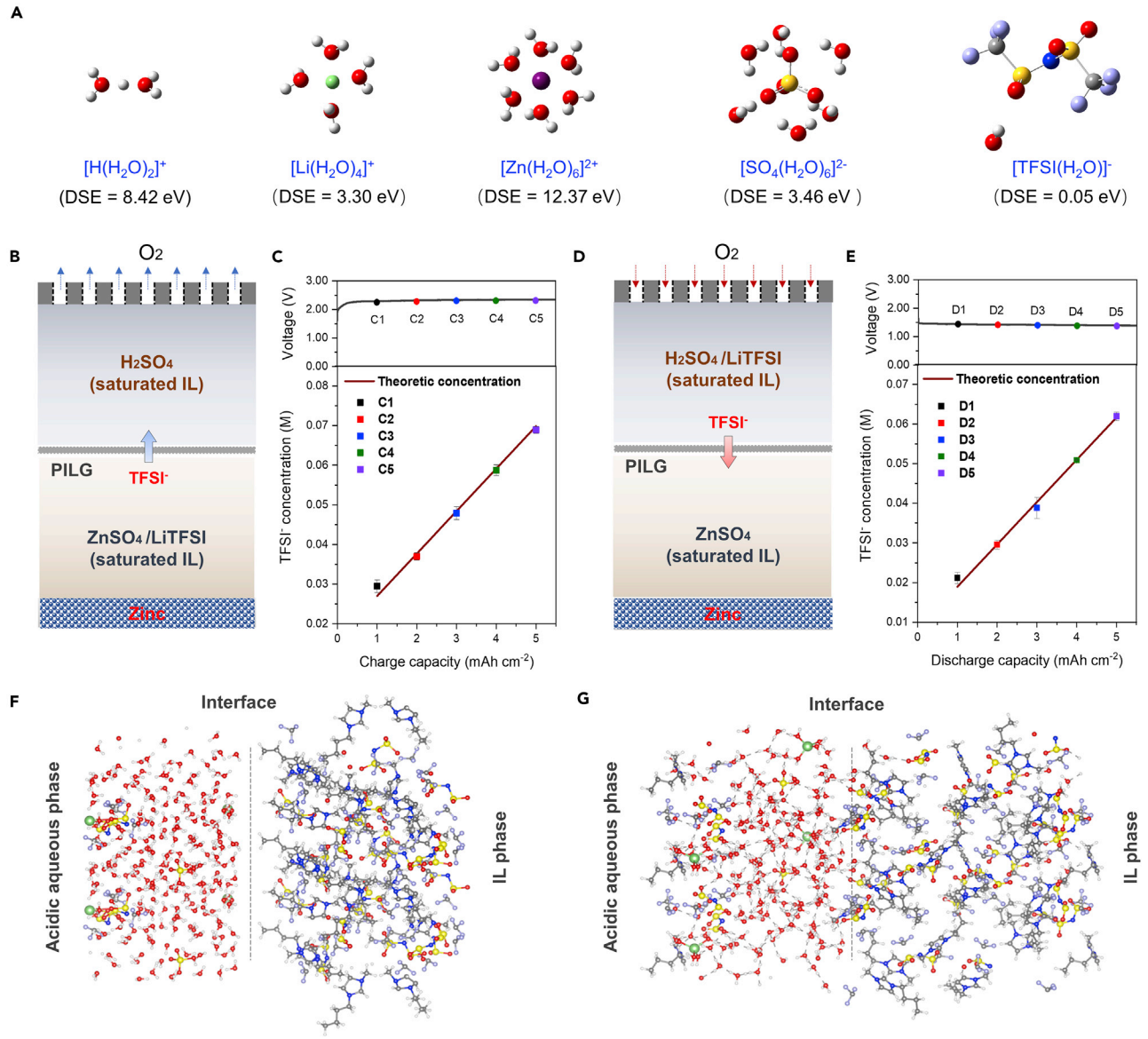


**Figure 3. $TFSI^-$-conducting process**

(A) Optimized geometries and the corresponding desolvation energies for the solvated $H^+$, $Li^+$, $Zn^{2+}$, $SO_4^{2-}$, and $TFSI^-$ ions.

(B) Schematic diagram of the $TFSI^-$ ion conduction process upon charge.

(C) Charge curve for hybrid ZABs and corresponding concentration variation of $TFSI^-$ ions calculated from quantified $^{19}$F-NMR.

(D) Schematic diagram of the $TFSI^-$ ion conduction process upon discharge.

(E) Discharge curve of the hybrid ZABs and corresponding concentration variation of $TFSI^-$ ions calculated from quantified $^{19}$F-NMR.

(C and E) The $TFSI^-$ ion concentrations of different charge and discharge stages given in (C) and (E) are mean values, and error bars represent the standard deviation of three determinations.

(F and G) Schematic snapshots of AIMD simulations at 298 K for (F) 0 fs and (G) 10,000 fs to investigate the mixture between the acidic aqueous phase ($H_2SO_4$ + LiTFSI) and IL phase ([BMIM][TFSI]). The H, Li, C, N, S, O, and F atoms are represented by white, green, gray, blue, yellow, red, and light blue spheres, respectively.

To further confirm the $TFSI^-$-conducting process in the hybrid ZAB, $^{19}$F nuclear magnetic resonance ($^{19}$F-NMR) measurements were used to quantify the concentration of $TFSI^-$ ions in the anolyte and catholyte at different charge/discharge stages. Upon charging, $TFSI^-$ ions diffused from the anolyte to the catholyte; thus, a $TFSI^-$-free catholyte was used to measure the concentration of $TFSI^-$ ions in the

Please cite this article in press as: Cui et al., A high-voltage and stable zinc-air battery enabled by dual-hydrophobic-induced proton shuttle shielding, Joule (2022), https://doi.org/10.1016/j.joule.2022.05.019



catholyte (Figure 3B). However, a $TFSI^-$-free anolyte was used upon discharge (Figure 3D). As mentioned above, the IL was dissolved in the catholyte and anolyte in trace amounts, and its dissolution could be completely suppressed by the IL-saturated electrolyte (Figure S19A). Thus, the IL-saturated anolyte and catholyte were quantified by $^{19}$F-NMR to reduce error (Figure S22). Upon charging, the concentration of the $TFSI^-$ ions in the catholyte increased with increasing capacity and was highly consistent with its theoretical value (Figure 3C; Figures S23A and S23C). The same process also occurred during discharge (Figure 3E; Figures S23B and S23D), meaning that the $TFSI^-$-conducting process dominated the charge transfer process. Furthermore, we performed *ab initio* molecular dynamics (AIMD) simulations to investigate the interface between the hydrophobic IL and the aqueous electrolytes (acidic aqueous catholyte of Figure 3F and neutral aqueous anolyte of Figure S24A). However, the states of phase separation remained almost unchanged even after running for 10,000 fs, demonstrating that water molecule or hydrophilic ion is unable to permeate the IL phase (Figures 3G and S24B).

## Cell performance

To estimate the battery performance, we then assembled the hybrid ZAB with the PILG. Compared with alkaline ZAB, the hybrid ZAB showed a higher OCV (~1.78 V; Figure 4A) due to its higher theoretical voltage. At a current density of 0.50 mA $cm^{-2}$, the hybrid ZAB exhibited a working voltage of ~1.55 V with a high energy efficiency of ~70.0% (Figure 4B). Note that the polarization potential of the hybrid ZAB increases with enhanced current density. As a result, the hybrid ZAB showed a discounted voltage of ~1.21 V at a current density of 10.0 mA $cm^{-2}$ (Figure 4B). The increased polarization was mainly caused by the sluggish kinetics of the OER/ORR in acidic electrolyte, since the total overpotential of the OER and ORR of the hybrid ZAB reached a high level of ~1.10 V and increased with cycling, whereas the Zn anode showed a stable overpotential of ~0.37 V (Figure S25). Even so, the hybrid ZABs still exhibited the higher working voltages and the similar energy efficiencies compared with the alkaline ZABs (Figure S26). Benefiting from the neutral anolyte that allowed the high reversibility of the Zn metal, the hybrid ZAB delivered a high discharge capacity of 802.3 mAh $g^{-1}$ based on Zn anode (theoretical capacity: 820.0 mAh $g^{-1}$) at a current density of 0.5 mA $cm^{-2}$ (Figure 4C). Even at a high current density of 10.0 mA $cm^{-2}$, it exhibited a discharge capacity of 798.0 mAh $g^{-1}$, corresponding to a high Zn utilization of 97.3%. In contrast, owing to the severe corrosion of the Zn anode in a strong alkaline environment (Figure S27), the alkaline ZAB only showed a low Zn utilization of 79.4% at 0.5 mA $cm^{-2}$, which decreased to 64.3% at 10.0 mA $cm^{-2}$. The high Zn utilization enabled the hybrid ZAB to have superior capacity (802.3 mAh $g^{-1}$) and energy density (1,243.6 Wh $kg^{-1}$) based on Zn anode; these values are higher than those of reported alkaline ZABs (Table S5). More importantly, the hybrid ZAB exhibited a potential capability for long-term cycling and operated stably for 2,000.0 h at 0.5 mA $cm^{-2}$ without obvious degradation (Figure 4D). It should be highlighted that the pH of the anolyte in the hybrid ZAB decreased slightly from 5.41 to 4.52 after cycling for 2,000.0 h, confirming the excellent proton-shielding capability of the PILG. In contrast, the alkaline ZAB, at the same current density, only afforded a cycle life of 136.0 h. Moreover, even at increased current densities of 1.0, 2.0, 5.0, and 10.0 mA $cm^{-2}$, the hybrid ZABs still had a longer lifespan than the alkaline ZABs (Figure S28) and a cycle performance comparable with those of reported aqueous ZABs (Table S6).

To reveal the origin of the performances of different ZABs, the dead ZABs were disassembled for failure analysis. An exhausted metallic Zn source (left inset of Figure 4D) and $K_2CO_3$- and ZnO-covered air cathodes (Figures 4G, S29C, and S29D) were

Please cite this article in press as: Cui et al., A high-voltage and stable zinc-air battery enabled by dual-hydrophobic-induced proton shuttle shielding, Joule (2022), https://doi.org/10.1016/j.joule.2022.05.019





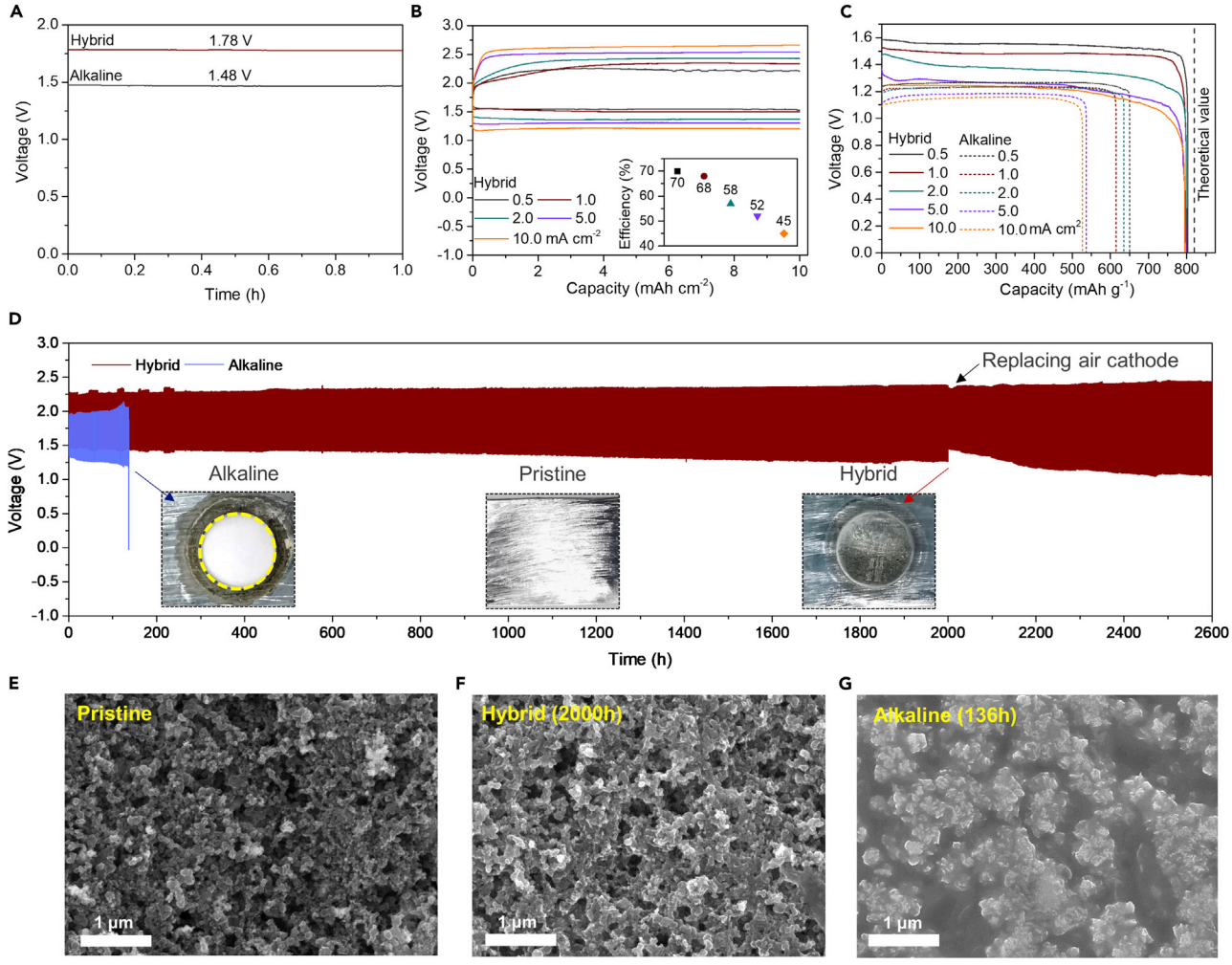


**Figure 4. Performances of the hybrid ZAB and alkaline ZAB**

(A) OCVs maintained within 1 h.

(B) Discharge and charge curves at different current densities (0.5, 1.0, 2.0, 5.0, and 10.0 mA $cm^{-2}$). Inset: energy efficiencies at different current densities.

(C) Discharge capacity curves based on the Zn anode at different currents (0.5, 1.0, 2.0, 5.0, and 10.0 mA $cm^{-2}$).

(D) Cycling performance at a discharge/charge current density of 0.5 mA $cm^{-2}$ for 1 h per cycle. Inset: photographs of the Zn anode from a dead ZAB.

(E–G) SEM images of air cathodes before and after cycling for 2,000.0 h and 136.0 h in hybrid and alkaline ZABs, respectively (scale bar, 1 μm).

detected in the alkaline ZAB after cycling for 136.0 h; these were responsible for the ultimate failure of the alkaline ZAB, further confirmed by the refreshed alkaline ZAB (Figure S30). By comparison, in the failed hybrid ZAB, the Zn anode remained intact (right inset of Figure 4D), and the microstructure of the air cathode remained almost unchanged even after long operation for 2,000.0 h (Figures 4E and 4F; Figures S29A, S29B and S29D). Furthermore, before the exhaustion of the Zn source, the Zn anode showed the obvious dendritic growth in the alkaline ZAB (Figures S31A and S31B), whereas a flat surface of Zn anode was observed in the hybrid ZAB (Figure S31C). These results suggested that the proposed hybrid ZAB concept could surmount the core challenges plaguing alkaline ZABs. However, owing to severe corrosion of the carbon matrix in acidic electrolytes upon the charging process,[39–41] the localized microporous layer (MPL) was exfoliated from the backing paper (carbon fiber layer) of the air cathode (Figure S29E), in turn causing catholyte leakage. Thus, the

Please cite this article in press as: Cui et al., A high-voltage and stable zinc-air battery enabled by dual-hydrophobic-induced proton shuttle shielding, Joule (2022), https://doi.org/10.1016/j.joule.2022.05.019



unstable carbon-based air cathode rather than the hybrid battery prototype was responsible for the failure of the hybrid ZAB. Therefore, refreshing the air cathode would enable the dead hybrid ZAB to work normally for another 600.0 h (Figure 4D). This result further demonstrates the feasibility of the proposed hybrid ZAB system, and its lifespan could be further prolonged by employing a more advanced air cathode (beyond the topic of the work; highly efficient acidic catalysts can decrease the overpotential of ORR/OER, thus increasing the working voltage, rate capability, and energy efficiency of hybrid ZABs. On the other hand, robust ORR/OER catalysts can prevent/alleviate the catalyst dissolution and carbon corrosion problems, which could significantly improve the cycling performances of hybrid ZAB). To demonstrate the simplicity of fabrication and applicability of this battery, a scaled-up hybrid ZAB was assembled and the regulable energy density was predicted based on the highly soluble $TFSI^-$-based salts,[42–44] which exhibited the electrochemical performance similar to that of the small one and drove a fan to rotate (Figure S32).

## DISCUSSION

To overcome the severe electrochemical irreversibility of conventional ZABs originating from strong alkaline electrolytes, we propose a hybrid ZAB with an acidic air cathode to prevent detrimental side reactions and precipitations and a neutral Zn anode to permit highly reversible Zn stripping/plating behavior and develop a dual-hydrophobic membrane to give full play to the advantages of hybrid neutral-acidic system. Using this hybrid ZAB as an example, the PILG effectively prevents the crossover of protons and selectively transport hydrophobic $TFSI^-$ ions to maintain ionic conduction inside the hybrid battery. Additionally, from our perspective, perhaps more important than the hybrid ZAB is the fact that the proposed proton-shuttle-shielding and hydrophobic-ion-conducting strategy is able to solve the mostly common cross-contamination of electrolytes-hybrid systems. This strategy creates a development direction for high-performance energy storage systems via decoupling the high-potential acidic redox couples and stable neutral Zn anode (Figure 5A). Two representative examples, described in Figures 5B and 5C, are the hybrid Zn-manganese (Mn) battery based on solid-liquid transition reaction of acidic $MnO_2/Mn^{2+}$ redox couple and hybrid Zn-bromine (Br) battery based on liquid phase reaction of acidic $Br_2/Br^-$ redox couple. Notably, such hybrid batteries are expected to achieve the long cycle life and potential high energy density.

## EXPERIMENTAL PROCEDURES

### Resource availability

#### *Lead contact*

Further information and requests for resources should be directed to and will be fulfilled by the lead contact, Xin-bo Zhang (xbzhang@ciac.ac.cn).

#### *Materials availability*

This study did not generate new unique reagents.

#### *Data and code availability*

The datasets generated in this study are available from the lead contact on reasonable request.

### Materials and methods

#### *Materials preparation*

Zinc sulfate heptahydrate ($ZnSO_4 \cdot 7H_2O$), [BMIM][TFSI] and PVDF-HFP were obtained from Sigma Aldrich. LiTFSI, potassium hydroxide (KOH), zinc acetate [$Zn(Ac)_2$], and isopropanol were obtained from Aladdin. Acetone ($CH_3COCH_3$) and

Please cite this article in press as: Cui et al., A high-voltage and stable zinc-air battery enabled by dual-hydrophobic-induced proton shuttle shielding, Joule (2022), https://doi.org/10.1016/j.joule.2022.05.019





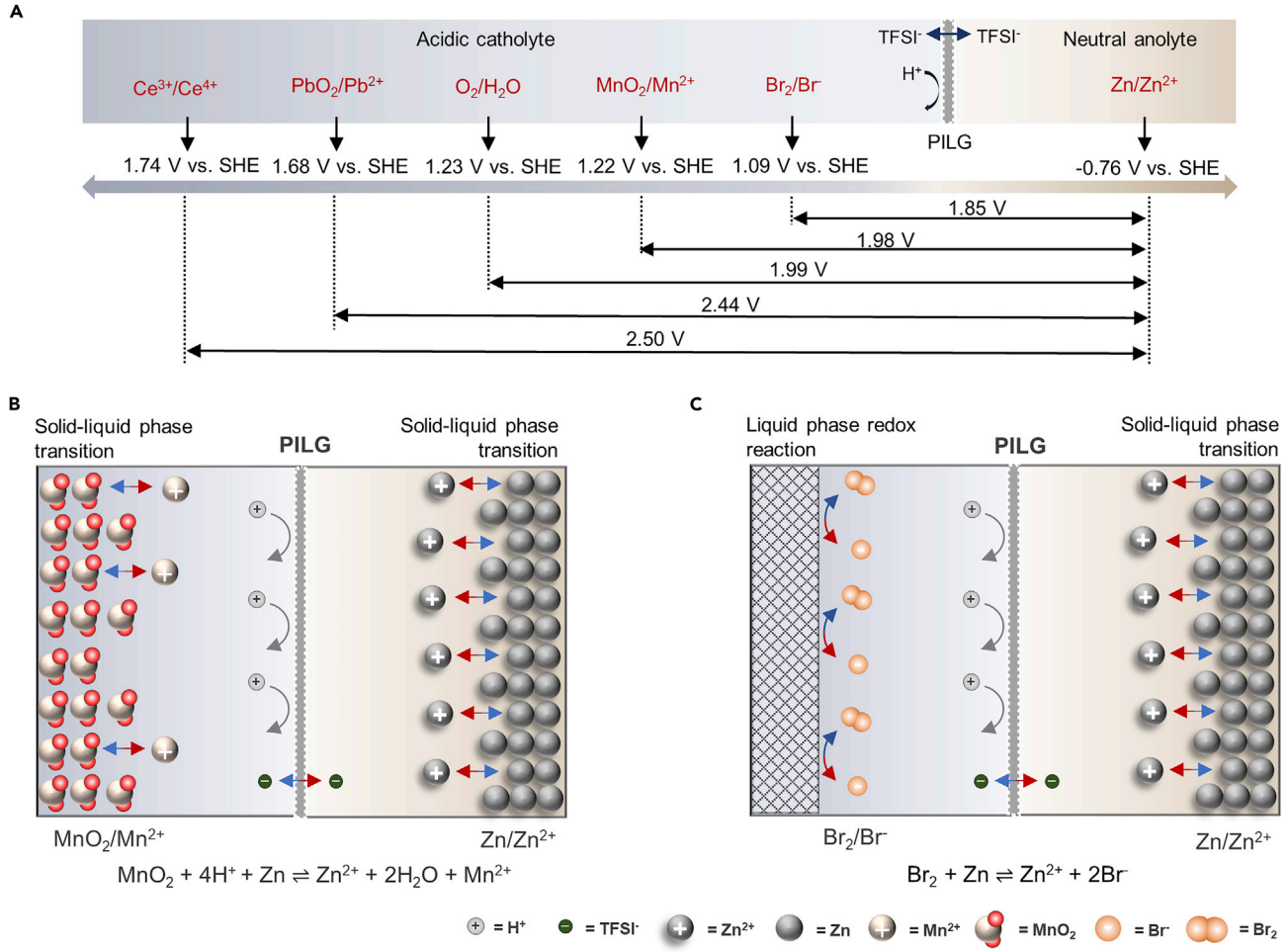


**Figure 5. Preferred cell configurations for decoupled aqueous Zn batteries with neutral anolyte and acidic catholyte based on PILG**

(A) Decoupling aqueous Zn batteries with the high-potential acidic redox pairs and highly reversible neutral Zn anode.

(B and C) Schematic diagrams of the typical (B) hybrid Zn-Mn and (C) hybrid Zn–Br batteries based on the proton-shuttle-shielding and hydrophobic $TFSI^-$-conducting PILG.

$H_2SO_4$ were obtained from Xilong Scientific. Zinc bis(trifluoromethylsulfonyl)imide [$Zn(TFSI)_2$] was obtained from J&K Scientific. Commercial 20% Pt/C, 40% Pt/C and $IrO_2$, obtained from Premetek, were used as catalysts. The commercial IEMs of Fumasep FAB-PK-130 and Nafion N117 were obtained from SCI Materials Hub. Graphene (99% purity, single layer ratio of 80%, 0.8 nm thickness and diameter of 0.5–5 μm) was purchased from Nanjing XFNANO Materials Tech, China. Gas diffusion layers of GDL 340 (CeTech) and SGL 39BC (Sigracet) and Nafion dispersion (Nafion D520) were obtained from SCI Materials Hub. Zn foil (100 μm thickness) and Zn powder were obtained from the SCI Materials Hub.

### *Membrane preparation*

Fumasep FAB-PK-130 and Nafion N117 were used as the AEM and the CEM, respectively, which were soaked separately in 3 M $Li_2SO_4$ solution for 24 h and thoroughly washed with DI water before use. The ILG was fabricated using an automatic ball-milling system for 1 h with different contents of graphene in 1 g of [BMIM][TFSI]. The PILG was prepared by the following steps. First, 1 g of PVDF-HFP was added to 7 mL of $CH_3COCH_3$ and stirred for 2 h to produce a transparent and

Please cite this article in press as: Cui et al., A high-voltage and stable zinc-air battery enabled by dual-hydrophobic-induced proton shuttle shielding, Joule (2022), https://doi.org/10.1016/j.joule.2022.05.019



homogeneous solution. Subsequently, ILG containing 1 g of IL and 15 mg of graphene was added, and the mixed solution was stirred for 3 h and sonicated for 2 h. After stirring for 3 h again, the resulting solution was uniformly poured onto a glass substrate by drop casting and then dried at 25°C for 24 h to remove the solvent and allow isothermal crystallization of the polymer substrate. Except for the ball-milling process, the PIL was obtained using the same method as the PILG by the direct addition of [BMIM][TFSI] to a homogeneous mixture of PVDF-HFP and $CH_3COCH_3$, followed by stirring, sonication, stirring and drop casting.

### *Preparation of the Zn anode and air cathode*

The Zn foil anode was cut into a suitable strip with an electrode area of 0.5 $cm^{-2}$ and an average mass of approximately 37 mg. The Zn power anode was prepared by mixing Zn power, conductive carbon black (Super P; TIMCAL Graphite & Carbon) and polyvinylidene difluoride binder (PVDF; Solvay) in a weight ratio of 90:5:5 using N-methyl-2-pyrrolidone (NMP; Aladdin) as the solvent and dispersant, and the mixed slurry was coated on Cu foil and then dried at 80°C for 24 h. Zn power electrodes with an anode area of 0.5 $cm^{-2}$ and an average mass of approximately 9–11 mg were used in the discharge performance and were used to calculate the Zn utilization, specific capacity and energy density.

The preparation of the GDL 340 Pt/C20 + $IrO_2$ electrode was as follows. 12.5 mg of 20% Pt/C, 2.5 mg of $IrO_2$ and 150 μL Nafion dispersion were mixed in 3 mL isopropanol/water solution with a volume ratio of 3:1, and the mixed solution was then sonicated for 40 min. The resulting solution was uniformly coated on GDL 340, which had an area of 25 $cm^2$, and then dried at room temperature for 24 h to remove the isopropanol/water solution. The achieved GDL 340 Pt/C20 + $IrO_2$ electrodes were cut with average loads of 0.5 mg $cm^{-2}$ 20% Pt/C and 0.1 mg $cm^{-2}$ IrO2 and then used to test the cycling performance of the ZABs at a small current density of 0.5 mA $cm^{-2}$. The preparation process of the SGL 39BC PtC40 + $IrO_2$ electrode was similar to that of GDL 340 Pt/C20 + $IrO_2$. The difference was that the SGL 39BC PtC40 + $IrO_2$ electrode had average loadings of 0.5 mg $cm^{-2}$ of 40% Pt/C and 0.5 mg $cm^{-2}$ of $IrO_2$, which were used in ZABs to test the OCVs, discharge performance, and cycle performance at 1.0, 2.0, 5.0 and 10.0 mA $cm^{-2}$.

### *Cell assembly*

Using CR2032 coin cells, the CE of Zn stripping/plating behavior in different electrolytes was determined, in which Zn foil and Ti foil electrodes were separated by glass fiber (GF/A, Whatman) using ~130 μL of electrolyte. A homemade Swagelok-type cell with a flexible design that can be assembled and disassembled was used for pH monitoring, and two-electrode and three-electrode systems with anode and cathode areas of 0.5 $cm^{-2}$ were used. Using homemade cells, the prepared Zn anode and air cathode were assembled. Specifically, the AEM-based hybrid ZABs used 1.6 mL of anolyte (0.5 M $ZnSO_4$) and 1.6 mL of catholyte (0.5 M $H_2SO_4$) separated by an AEM. The CEM-based hybrid ZABs used 1.6 mL of anolyte (0.5 M $ZnSO_4$ + 0.5 M $Li_2SO_4$) and 1.6 mL of catholyte (0.5 M $H_2SO_4$ + 0.5 M $Li_2SO_4$) separated by a CEM. Hybrid ZABs with PIL or PILG membranes used 1.6 mL of anolyte (0.5 M $ZnSO_4$ + 1 M LiTFSI) and 1.6 mL of catholyte (0.5 M $H_2SO_4$ + 1 M LiTFSI) separated by the PIL or PILG. In addition, the alkaline ZABs used 1.6 mL of electrolyte (6 M KOH + 0.2 M $Zn(Ac)_2$) and were assembled using a single reaction chamber.

### *Materials characterization*

$^{19}$F-NMR was recorded on a Bruker (*AVANCE III, HD* 500 MHz) NMR spectrometer. X-ray diffraction (XRD) data were collected on a Bruker D8 Focus powder X-ray

diffractometer using Cu Kα radiation. SEM was carried out with a field emission scanning electron microanalyser (Hitachi S4800). Transmission electron microscopy (TEM) and high-resolution TEM (HRTEM) were performed on an FEI Tecnai G2 S-Twin instrument with a field emission gun operating at 200 kV. Attenuated total reflection FTIR measurements were carried out using a Thermo (Nicolet 6700) system at 4 $cm^{-1}$ resolution. Electrochemical impedance spectroscopy (EIS) was performed over a frequency range from 7 –100 MHz at an AC amplitude of 10 mV. Linear polarization curves were collected by a Biologic VMP3 system at 0.1 mV $s^{-1}$ using Zn foil as the working electrode, Ag/AgCl as the reference electrode and Pt foil as the counter electrode. Charge-discharge tests of the batteries were carried out using the galvanostatic method on a Land instrument.

### *Theoretical methods*

All the calculations for $SO_4^{2-}$, $TFSI^-$, $Zn^{2+}$, $H^+$, $Li^+$, and their solvated structures were carried out in the Gaussian 16 software package. The structures and thermal corrections to the Gibbs free energy and complexes were optimized at the level of B3LYP-D3(BJ)/6-311+g(d). All the optimized structures were confirmed by the absence of a negative frequency. High-accuracy single-point energy calculations were performed at the B2PLYP-D3(BJ)/def2-TZVP level. The molecular polarity indices (MPIs) and electrostatic potential were calculated by Multiwfn, and the latter was visualized by visual molecular dynamics (VMD).[45–47]

The calculations of absorption energy between graphene and $BMIM^+$, as well as PVDF-HFP and $BMIM^+$, were implemented using the Vienna *ab initio* simulation package code (VASP) with the generalized gradient approximation (GGA) expressed by the Perdew-Burke-Ernzerhof (PBE) functional.[48,49] The valence electron-ion interaction was described using the projector-augmented plane wave (PAW).[50,51] A 400 eV cutoff with van der Waals (vDW) corrections was used in the absorption models. The convergence criteria of energy and force for structural optimization were set as $10^{-5}$ eV and 0.02 eV $Å^{-1}$. The absorption energy was calculated based on $\Delta E_{ab} = E_{tot} - E_{sub} - E_{abs}$, where $E_{tot}$ is the total energy of the substrate and absorbate. The energy of the graphene substrate or PVDF-HFP substrate is represented as $E_{sub}$. In addition, the $E_{abs}$ is regarded as the energy of $BMIM^+$.

AIMD simulations were carried out by using VASP. In all the simulations, the models were strictly constructed according to the measured results from the experiment. Over the course of the AIMD simulations with a plane-wave energy cutoff of 400 eV, the four simulated systems were all large enough to utilize a Monkhorst-Pack k-point mesh grid scheme (1 × 1 × 1). A canonical (NVT) ensemble was performed by using a Nose-Hoover thermostat at 298 K.[52–54] The total AIMD simulation time for each system was 10 ps with a time step of 1 fs. The snapshots of the systems were twice as large as the simulation box.

## SUPPLEMENTAL INFORMATION

Supplemental information can be found online at https://doi.org/10.1016/j.joule.2022.05.019.

## ACKNOWLEDGMENTS

This work was financially supported by the National Natural Science Foundation of China (21725103), National Key R&D Program of China (2017YFA0206704), Key Research Program of the Chinese Academy of Sciences (ZDRW-CN-2021-3), Changchun Science and Technology Development Plan Funding Project (21ZY06), and

China Postdoctoral Science Foundation (2020M681035). Supercomputing USTC and Network and Computing Center, Changchun Institute of Applied Chemistry, and Chinese Academy of Sciences are acknowledged for computational support.

## AUTHOR CONTRIBUTIONS

Y.-f.C., Y.-h.Z., and X.-b.Z. proposed the concept and designed the experiment. Y.-f.C. and Y.-h.Z carried out the experiments and characterizations. J.-y.D and K.L. conducted the theoretical calculations. Y.-l.Z. shared valuable experience in ILs. X.-b.Z., G.H., Y.-f.C., Y.-h.Z., J.-y.D., and W.-q.L. contributed to results and co-wrote the manuscript, and all authors discussed the results and reviewed the manuscript.

## DECLARATION OF INTERESTS

The authors declare no competing interests.

Received: March 30, 2022
Revised: May 4, 2022
Accepted: May 26, 2022
Published: June 20, 2022

## REFERENCES

1. Li, Y., and Dai, H. (2014). Recent advances in zinc-air batteries. Chem. Soc. Rev. *43*, 5257–5275.
2. Sun, W., Wang, F., Zhang, B., Zhang, M., Küpers, V., Ji, X., Theile, C., Bieker, P., Xu, K., Wang, C., et al. (2021). A rechargeable zinc-air battery based on zinc peroxide chemistry. Science *371*, 46–51.
3. Wang, H.-F., and Xu, Q. (2019). Materials design for rechargeable metal-air batteries. Matter *1*, 565–595.
4. Stock, D., Dongmo, S., Janek, J., and Schröder, D. (2019). Benchmarking anode concepts: the future of electrically rechargeable zinc-air batteries. ACS Energy Lett *4*, 1287–1300.
5. Gu, P., Zheng, M., Zhao, Q., Xiao, X., Xue, H., and Pang, H. (2017). Rechargeable zinc-air batteries: a promising way to green energy. J. Mater. Chem. A *5*, 7651–7666.
6. Yi, J., Liang, P., Liu, X., Wu, K., Liu, Y., Wang, Y., Xia, Y., and Zhang, J. (2018). Challenges, mitigation strategies and perspectives in development of zinc-electrode materials and fabrication for rechargeable zinc-air batteries. Energy Environ. Sci. *11*, 3075–3095.
7. Zhang, J., Zhou, Q., Tang, Y., Zhang, L., and Li, Y. (2019). Zinc-air batteries: are they ready for prime time? Chem. Sci. *10*, 8924–8929.
8. Zhao, Z., Fan, X., Ding, J., Hu, W., Zhong, C., and Lu, J. (2019). Challenges in zinc electrodes for alkaline zinc-air batteries: obstacles to commercialization. ACS Energy Lett *4*, 2259–2270.
9. Luo, H., Liu, B., Yang, Z., Wan, Y., and Zhong, C. (2022). The trade-offs in the design of reversible zinc anodes for secondary alkaline batteries. Electrochem. Energy Rev. *5*, 187–210.
10. Zhong, Y., Liu, B., Zhao, Z., Shen, Y., Liu, X., and Zhong, C. (2021). Influencing factors of performance degradation of zinc-air batteries exposed to air. Energies *14*, 2607.
11. Pan, J., Xu, Y.Y., Yang, H., Dong, Z., Liu, H., and Xia, B.Y. (2018). Advanced architectures and relatives of air electrodes in Zn-air batteries. Adv. Sci. (Weinh) *5*, 1700691.
12. Zhou, T., Zhang, N., Wu, C., and Xie, Y. (2020). Surface/interface nanoengineering for rechargeable Zn-air batteries. Energy Environ. Sci. *13*, 1132–1153.
13. Chen, X., Zhou, Z., Karahan, H.E., Shao, Q., Wei, L., and Chen, Y. (2018). Recent advances in materials and design of electrochemically rechargeable zinc-air batteries. Small *14*, e1801929.
14. Parker, J.F., Chervin, C.N., Pala, I.R., Machler, M., Burz, M.F., Long, J.W., and Rolison, D.R. (2017). Rechargeable nickel-3D zinc batteries: an energy-dense, safer alternative to lithium-ion. Science *356*, 415–418.
15. Parker, J.F., Nelson, E.S., Wattendorf, M.D., Chervin, C.N., Long, J.W., and Rolison, D.R. (2014). Retaining the 3D framework of zinc sponge anodes upon deep discharge in Zn-air cells. ACS Appl. Mater. Interfaces *6*, 19471–19476.
16. Wang, K., Pei, P., Ma, Z., Chen, H., Xu, H., Chen, D., and Wang, X. (2015). Dendrite growth in the recharging process of zinc-air batteries. J. Mater. Chem. A *3*, 22648–22655.
17. Hao, J., Li, X., Zeng, X., Li, D., Mao, J., and Guo, Z. (2020). Deeply understanding the Zn anode behaviour and corresponding improvement strategies in different aqueous Zn-based batteries. Energy Environ. Sci. *13*, 3917–3949.
18. Pan, H., Shao, Y., Yan, P., Cheng, Y., Han, K.S., Nie, Z., Wang, C., Yang, J., Li, X., Bhattacharya, P., et al. (2016). Reversible aqueous zinc/manganese oxide energy storage from conversion reactions. Nat. Energy *1*, 1–7.
19. Zhang, N., Cheng, F., Liu, Y., Zhao, Q., Lei, K., Chen, C., Liu, X., and Chen, J. (2016). Cation-deficient spinel $ZnMn_2O_4$ cathode in $Zn(CF_3SO_3)_2$ electrolyte for rechargeable aqueous Zn-Ion battery. J. Am. Chem. Soc. *138*, 12894–12901.
20. Zheng, J., Bock, D.C., Tang, T., Zhao, Q., Yin, J., Tallman, K.R., Wheeler, G., Liu, X., Deng, Y., Jin, S., et al. (2021). Regulating electrodeposition morphology in high-capacity aluminium and zinc battery anodes using interfacial metal-substrate bonding. Nat. Energy *6*, 398–406.
21. Ma, L., Schroeder, M.A., Borodin, O., Pollard, T.P., Ding, M.S., Wang, C., and Xu, K. (2020). Realizing high zinc reversibility in rechargeable batteries. Nat. Energy *5*, 743–749.
22. An, L., Zhang, Z., Feng, J., Lv, F., Li, Y., Wang, R., Lu, M., Gupta, R.B., Xi, P., and Zhang, S. (2018). Heterostructure-promoted oxygen electrocatalysis enables rechargeable zinc-air battery with neutral aqueous electrolyte. J. Am. Chem. Soc. *140*, 17624–17631.
23. Li, Z., Pan, M.S., Su, L., Tsai, P.-C., Badel, A.F., Valle, J.M., Eiler, S.L., Xiang, K., Brushett, F.R., and Chiang, Y.-M. (2017). Air-breathing aqueous sulfur flow battery for ultralow-cost long-duration electrical storage. Joule *1*, 306–327.
24. Yu, X., and Manthiram, A. (2017). A voltage-enhanced, low-cost aqueous iron-air battery enabled with a mediator-ion solid electrolyte. ACS Energy Lett *2*, 1050–1055.
25. Zhong, C., Liu, B., Ding, J., Liu, X., Zhong, Y., Li, Y., Sun, C., Han, X., Deng, Y., Zhao, N., et al. (2020). Decoupling electrolytes towards stable and high-energy rechargeable aqueous zinc-manganese dioxide batteries. Nat. Energy *5*, 440–449.
26. Gu, S., Gong, K., Yan, E.Z., and Yan, Y. (2014). A multiple ion-exchange membrane design for redox flow batteries. Energy Environ. Sci. *7*, 2986–2998.

27. Gong, K., Ma, X., Conforti, K.M., Kuttler, K.J., Grunewald, J.B., Yeager, K.L., Bazant, M.Z., Gu, S., and Yan, Y. (2015). A zinc-iron redox-flow battery under $100 per kW h of system capital cost. Energy Environ. Sci. *8*, 2941–2945.

28. Das, S., Imoto, S., Sun, S., Nagata, Y., Backus, E.H.G., and Bonn, M. (2020). Nature of excess hydrated proton at the water-air interface. J. Am. Chem. Soc. *142*, 945–952.

29. Marcus, Y. (2009). Effect of ions on the structure of water: structure making and breaking. Chem. Rev. *109*, 1346–1370.

30. Wang, X.B., Yang, X., Nicholas, J.B., and Wang, L.S. (2001). Bulk-like features in the photoemission spectra of hydrated doubly charged anion clusters. Science *294*, 1322–1325.

31. Xu, Y., Cai, P., Chen, K., Ding, Y., Chen, L., Chen, W., and Wen, Z. (2020). High-voltage rechargeable alkali-acid Zn–$PbO_2$ hybrid battery. Angew. Chem. Int. Ed. Engl. *59*, 23593–23597.

32. Yang, L., Zeng, J., Ding, B., Xu, C., and Lee, J.Y. (2016). Lithium salt inclusion as a strategy for improving the $Li^+$ conductivity of nafion membranes in aprotic systems. Adv. Mater. Interfaces *3*, 1600660.

33. Schmidt-Rohr, K., and Chen, Q. (2008). Parallel cylindrical water nanochannels in nafion fuel-cell membranes. Nat. Mater. *7*, 75–83.

34. Zheng, Y., Ash, U., Pandey, R.P., Ozioko, A.G., Ponce-González, J., Handl, M., Weissbach, T., Varcoe, J.R., Holdcroft, S., Liberatore, M.W., et al. (2018). Water uptake study of anion exchange membranes. Macromolecules *51*, 3264–3278.

35. Armand, M., Endres, F., MacFarlane, D.R., Ohno, H., and Scrosati, B. (2009). Ionic-liquid materials for the electrochemical challenges of the future. Nat. Mater. *8*, 621–629.

36. Nordness, O., and Brennecke, J.F. (2020). Ion dissociation in ionic liquids and ionic liquid solutions. Chem. Rev. *120*, 12873–17902.

37. Shakourian-Fard, M., Jamshidi, Z., Bayat, A., and Kamath, G. (2015). Meta-hybrid density functional theory study of adsorption of imidazolium- and ammonium-based ionic liquids on graphene sheet. J. Phys. Chem. C *119*, 7095–7108.

38. Zhao, Y., and Hu, Z. (2013). Graphene in ionic liquids: collective van der Waals interaction and hindrance of self-assembly pathway. J. Phys. Chem. B *117*, 10540–10547.

39. Yi, Y., Tornow, J., Willinger, E., Willinger, M.G., Ranjan, C., and Schlögl, R. (2015). Electrochemical degradation of multiwall carbon nanotubes at high anodic potential for oxygen evolution in acidic media. ChemElectroChem *2*, 1929–1937.

40. Oh, H.S., Nong, H.N., Reier, T., Bergmann, A., Gliech, M., Ferreira de Araújo, J.F., Willinger, E., Schlögl, R., Teschner, D., and Strasser, P. (2016). Electrochemical catalyst-support effects and their stabilizing role for $IrO_x$ nanoparticle catalysts during the oxygen evolution reaction. J. Am. Chem. Soc. *138*, 12552–12563.

41. Massué, C., Pfeifer, V., Huang, X., Noack, J., Tarasov, A., Cap, S., and Schlögl, R. (2017). High-performance supported iridium oxohydroxide water oxidation electrocatalysts. ChemSusChem *10*, 1943–1957.

42. Suo, L., Borodin, O., Gao, T., Olguin, M., Ho, J., Fan, X., Luo, C., Wang, C., and Xu, K. (2015). Water-in-salt" electrolyte enables high-voltage aqueous lithium-ion chemistries. Science *350*, 938–943.

43. Wang, F., Borodin, O., Gao, T., Fan, X., Sun, W., Han, F., Faraone, A., Dura, J.A., Xu, K., and Wang, C. (2018). Highly reversible zinc metal anode for aqueous batteries. Nat. Mater. *17*, 543–549.

44. Patil, N., Cruz, C., Ciurduc, D., Mavrandonakis, A., Palma, J., and Marcilla, R. (2021). An ultrahigh performance zinc-organic battery using poly(catechol) cathode in $Zn(TFSI)_2$-based concentrated aqueous electrolytes. Adv. Energy Mater. *11*, 2100939.

45. Liu, Z., Lu, T., and Chen, Q. (2021). Intermolecular interaction characteristics of the all-carboatomic ring, cyclo[18]carbon: focusing on molecular adsorption and stacking. Carbon *171*, 514–523.

46. Lu, T., and Chen, F. (2012). Multiwfn: a multifunctional wavefunction analyzer. J. Comput. Chem. *33*, 580–592.

47. Humphrey, W., Dalke, A., and Schulten, K. (1996). VMD: visual molecular dynamics. J. Mol. Graphics *14*, 33–38.

48. Kresse, G., and Hafner, J. (1993). *Ab initio* molecular dynamics for liquid metals. Phys. Rev. B Condens. Matter *47*, 558–561.

49. Perdew, J.P., Burke, K., and Ernzerhof, M. (1996). Generalized gradient approximation made simple. Phys. Rev. Lett. *77*, 3865–3868.

50. Blöchl, P.E. (1994). Projector augmented-wave method. Phys. Rev. B Condens. Matter *50*, 17953–17979.

51. Kresse, G., and Joubert, D. (1999). From ultrasoft pseudopotentials to the projector augmented-wave method. Phys. Rev. B *59*, 1758–1775.

52. Nosé, S. (1984). A unified formulation of the constant temperature molecular dynamics methods. J. Chem. Phys. *81*, 511–519.

53. Nosé, S. (1991). Constant temperature molecular dynamics methods. Prog. Theor. Phys. Suppl. *103*, 1–46.

54. Hoover, W.G. (1985). Canonical dynamics: equilibrium phase-space distributions. Phys. Rev. A Gen. Phys. *31*, 1695–1697.